Nano Research

Open Access

Research Article

Engineered extracellular vesicles with multitargeted anti-microRNA for diabetes-induced cognitive impairment therapy

Xuetao Chen[1,2,§], Haixiang Sun[1,2,§], Zhicong Zhao[1,2], Junyi Che[3] ✉, Yan Bi[1,2] ✉, Yuanjin Zhao[3] ✉, and Jin Wang[1,2] ✉

[1] *Department of Endocrinology, Endocrine and Metabolic Disease Medical Center, Affiliated Hospital of Medical School, Nanjing Drum Tower Hospital, Nanjing University, Nanjing 210008, China*
[2] *Branch of National Clinical Research Centre for Metabolic Diseases, Nanjing 210023, China*
[3] *Department of Rheumatology and Immunology, Institute of Translational Medicine, Nanjing Drum Tower Hospital, Affiliated Hospital of Medical School, Nanjing University, Nanjing 210008, China*
[§] *Xuetao Chen and Haixiang Sun contributed equally to this work.*

Cite this article: *Nano Research*, **2026**, *19*, 94908479. https://doi.org/10.26599/NR.2026.94908479

ABSTRACT: RNA therapeutics have shown considerable promise in the treatment of various neurological disorders, while their effective delivery across the blood-brain barrier (BBB) and modulation of multiple microRNA pathological targets remains critical challenges. In this study, we developed a dual-engineered extracellular vesicle (EV) system for the target delivery of multiple microRNA inhibitors (anti-miRs) to the brain to treat diabetes-induced cognitive impairment. The engineered EVs were efficiently loaded with a panel of therapeutic anti-miRs and demonstrated effective synaptic recovery in primary neurons under synapse-losing conditions. *In vivo*, the system showed enhanced brain accumulation after intravenous injection. Furthermore, in a diabetic mouse model, treatment with this system significantly restored brain-derived neurotrophic factor (BDNF) and synaptic markers levels, leading to marked improvement in cognitive deficits. These findings underscore the potential of this EV-based platform as a brain-targeted strategy for microRNA-based therapeutics in neurodegenerative and metabolic central nervous system disorders.

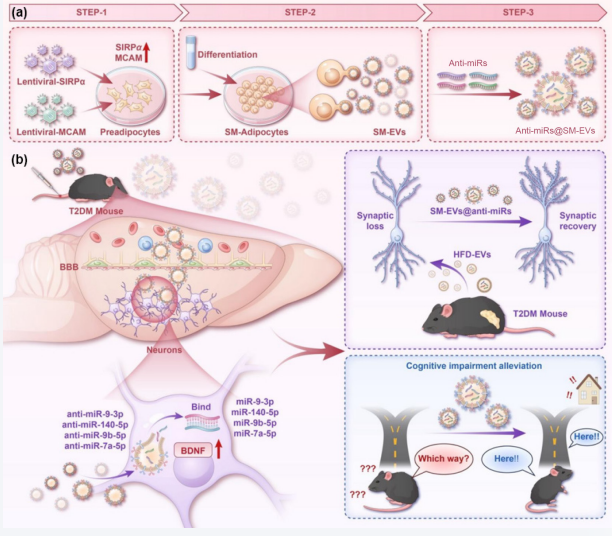

KEYWORDS: extracellular vesicle, microRNA inhibitor, brain, drug delivery, cognitive impairment, diabetes

1 Introduction

It is approximately 30% of individuals with diabetes exhibit cognitive decline, which progress at a rate nearly 50% faster than that observed during normal aging [1–4]. This deterioration affects multiple cognitive domains, including memory, executive function, and processing speed [5, 6]. Recent studies have revealed that visceral adipose tissue in patients with diabetes impairs synaptic plasticity in the hippocampus by delivering pathogenic microRNAs, such as miR-9-3p, miR-9b-5p, miR-140-5p, and miR-7a-5p, thereby exacerbating cognitive impairment. Moreover, this damage is difficult to reverse with conventional pharmacological treatments [7, 8]. Despite advances in targeting these pathogenic microRNAs [9–11], effective RNA-based therapies remain challenging [12–14]. Generally, RNA therapeutics face rapid enzymatic degradation and immune clearance following systemic administration [15, 16]. In addition, conventional nanocarrier delivery systems suffer from limited blood-brain barrier (BBB) penetration [17–20]. Furthermore, single-target approaches often fail due to the complex and multifactorial nature of neurodegenerative diseases [21–23]. Given these limitations

Received: December 9, 2025; **Revised:** January 21, 2026
Accepted: January 21, 2026

✉Address correspondence to Junyi Che, chejunyi01@163.com; Yuanjin Zhao, yjzhao@njglyy.com; Yan Bi, biyan@nju.edu.cn; Jin Wang, wangjin@smail.nju.edu.cn

[24–26], the development of effective brain-targeted, multifactorial therapeutic strategies represents a highly promising direction for diabetes-induced cognitive impairment [27–29].

Here, we propose a novel multi-engineered adipocyte-derived extracellular vesicle (EV) delivery system with four targeted anti-miRs (anti-miR-9-3p, anti-miR-9b-5p, anti-miR-140-5p, anti-miR-7a-5p) to the brain for the treatment of diabetic cognitive impairment, as schemed in Fig. 1. EVs are lipid bilayer particles secreted by cells that mediate intercellular communication. Engineered EVs, modified to carry specific cargos or targeting molecules, have emerged as promising tools for therapeutic delivery and disease intervention [30]. Various types of EVs, such as exosomes and apoptotic bodies, have shown promise in biomedical applications [31]. Advances in engineering strategies, including surface modification and cargo loading, have enhanced their potential for disease treatment, particularly in targeted and multifunctional therapies [32]. Our previous study discovered that adipocyte-derived EVs possess inherent brain-targeting capabilities, with preferential accumulation in the hippocampus region [8]. Further investigation identified signal regulatory protein α (SIRPα) and melanoma cell adhesion molecule (MCAM) on adipocyte derived EVs as key mediators facilitating their translocation across the BBB [33]. Based on these findings [34, 35], we envision that the overexpression of SIRPα and MCAM on adipocyte-derived EVs membranes holds great potential to enhance their BBB-penetrating capability [36–39], thus providing a promising brain-targeting platform for the delivery of anti-miRs in the treatment of diabetic cognitive decline [40, 41].

In this study, we fabricated the desired dually engineered, brain-targeted EV delivery platform loaded with four anti-miRs for cognitive impairment treatment (Fig. 1). To implement this concept, 3T3-L1 cells were transfected with lentiviral vectors to stably overexpress SIRPα and MCAM, followed by differentiation into adipocytes. SIRPα&MCAM-EVs (SM-EVs) were then isolated from these dual-engineered adipocytes and loaded with four anti-miRs via electroporation [42], yielding Anti-miRs@SM-EVs. We have demonstrated that the resultant Anti-miRs@SM-EVs exhibited high biocompatibility and effectively mitigated pathogenic factor-induced synaptic damage in primary neurons. Furthermore, *in vivo* fluorescence imaging revealed significantly enhanced brain accumulation of Anti-miRs@SM-EVs compared to conventional EVs, with the highest localization observed in the hippocampus. Based on these results, we have evaluated the therapeutic efficacy of Anti-miRs@SM-EVs in a diabetic mouse model. After four weeks of intravenous administration, Anti-miRs@SM-EVs markedly reversed synaptic injury, restored BDNF levels, and improved cognitive performance. These results suggest that our SM-EVs represent a promising brain-targeted delivery platform for treating diabetes-associated cognitive impairment and other central nervous system (CNS) disorders.

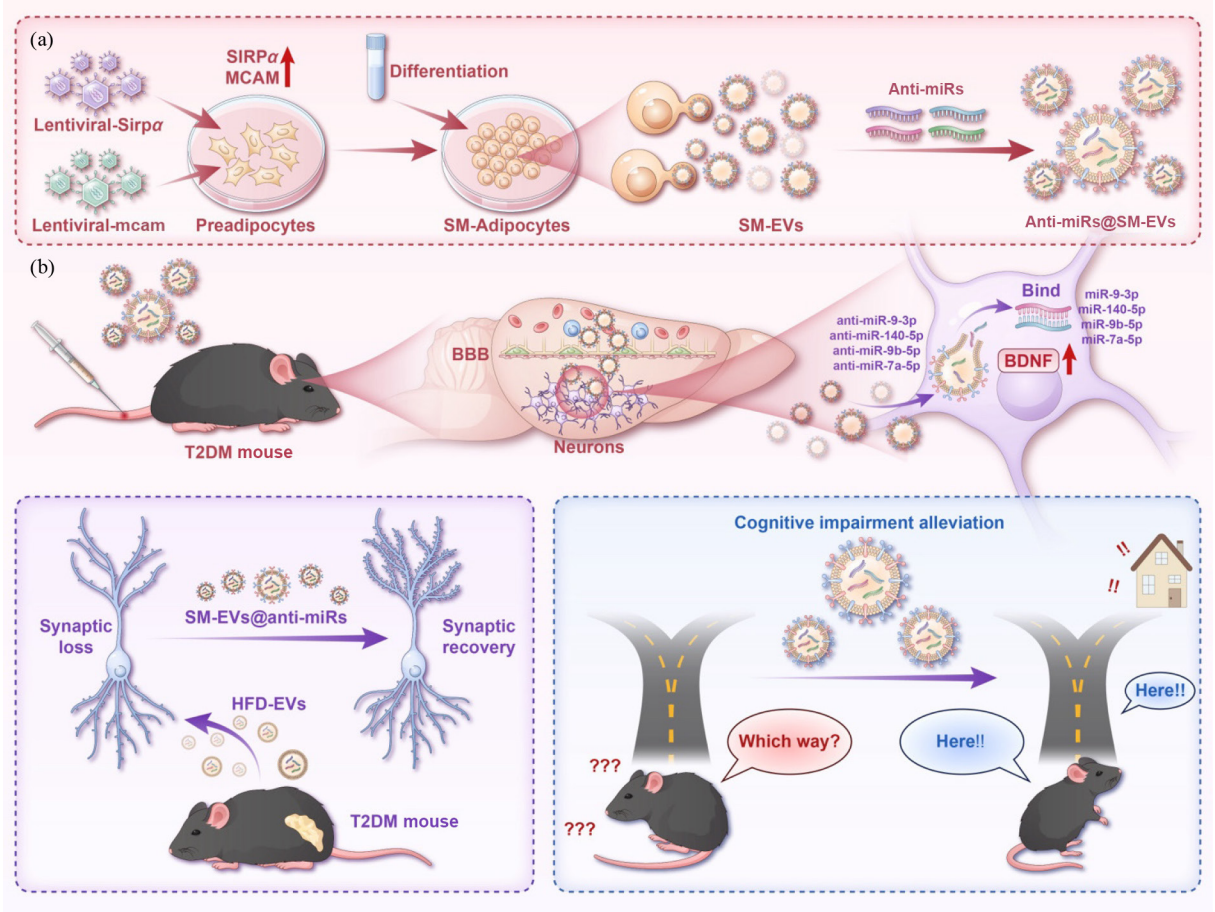

Figure 1 Schematic illustrations of Anti-miRs@SM-EVs for the treatment of diabetes-induced cognitive impairment. (a) Establishment of Anti-miRs@SM-EVs via lentiviral transduction and electroporation. (b) SM-EVs were intravenously delivered to diabetic mice. SIRPα and MCAM can help EVs cross BBB and target neurons, while four types of anti-miRs can eliminate pathogenic microRNA and restore BDNF level. This system can reverse synaptic loss and cognitive impairment.

2 Experimental

2.1 Materials

Recombinant lentiviruses overexpressing SIRPα and MCAM were obtained from Nanjing Zebrafish Biotechnology Co., Ltd. Dulbecco's modified eagle medium (DMEM) High Glucose (Cat. No. 11965092), NBCS (Newborn Calf Serum, Cat. No. 16010159), and Penicillin-Streptomycin solution (Cat. No. 15140122) were purchased from Thermo Fisher Scientific, Inc. 3 isobutyl 1 methylxanthine (IBMX, Cat. No. I5879), insulin (Cat. No. I6634) and dexamethasone (Cat. No. D4902) were purchased from Sigma Aldrich. Gene Pulser® Electroporation Buffer (Cat. No. 165 2676) and Gene Pulser®/MicroPulser™ Electroporation Cuvettes (4 mm gap, Cat. No. 1652088) were purchased from Bio Rad Laboratories, Inc. MicroRNA inhibitors were synthesized by GenScript. Primary antibodies against SIRPα (Cat. No. CY1259) were purchased from Abways, and against MCAM (Cat. No. BM4093) from Boster. SYN-1 antibody (Cat. No. 5297S) was obtained from CST. Anti MAP2 antibody (Cat. No. AB5392) and Anti BDNF antibody [EPR1292] (Cat. No. ab108319) were obtained from Abcam. Anti GAPDH antibody (monoclonal, Cat. No. 60004-1-Ig) was purchased from Proteintech. Enhanced chemiluminescence (ECL) Western Blotting Substrate (Cat. No. 180-501) was purchased from Tanon Science & Technology Co., Ltd. Immunofluorescence secondary antibodies (Cat. Nos. A-11094, S11227), phalloidin dye (Cat. No. R37110), DiD and DiR dyes (Cat. Nos. D7757, D12731) were purchased from Thermo Fisher Scientific Inc. 4',6-diamidino-2-phenylindole (DAPI), live/dead staining reagents, and the cell counting kit-8 (CCK-8) kit (Cat. Nos. C1006, C1371S, C0041) were obtained from Beyotime Biotechnology Co., Ltd. High-fat diet (Cat. No. D12492) was purchased from Research Diets.

2.2 Cell lines

3T3-L1 (RRID: CVCL_0123) cells were obtained from (Anwei-sci Cell Center, Shanghai, China (NO. AW-CM0038). HEK293T (RRID: VCL_0063) cells were purchased from Nanjing Zebrafish Biotech Co., Ltd. (NO. QuiCell-2342).

2.3 Animals

Male C57B6 mice were obtained from Hangzhou Ziyuan Laboratory Animal Technology Co., Ltd. All animal procedures adhered to institutional ethical standards. Mice were acclimatized under specific pathogen free (SPF) conditions for one week prior to experiments.

2.4 Lentiviral transduction and antibiotic selection

Both 3T3-L1 and HEK293T were seeded in six-well culture plates. The two viral particles were mixed and added to cells at 30%–50% confluence at a multiplicity of infection (MOI) of 20 each (total MOI 40). After 12 h of incubation, the medium was replaced with regular culture medium. 48 h after infection, selection was performed with 0.75 μg/mL puromycin and 1.5 μg/mL blasticidin, and maintained for 5–7 days until all uninfected control cells were eliminated. Successfully transduced cells were expanded for further experiments and verified for target gene expression via Western blot and confocal laser scanning microscopy (CLSM).

2.5 Isolation and characterization of EVs

EVs were harvested from mature adipocytes using sequential centrifugation and ultracentrifugation steps. Supernatants were subjected to centrifugation at 300*g* for 10 min to remove cells, 2000*g* for 20 min remove debris, and 10,000*g* for 30 min to remove large vesicles. Then the supernatant was ultracentrifuged at 110,000g for 70 min at 4 °C, and the pellet was resuspended and recentrifuged under the same conditions. For morphology, EVs were stained negatively with 2% phosphotungstic acid after adsorption to a carbon-coated copper grid, then imaged by transmission electron microscopy (TEM) (JEM-1230) at 80 kV.

2.6 Loading of anti-miRs into EVs via electroporation

To load anti-miRs into EVs, electroporation was carried out using a modified protocol. Approximately 50–100 μg of purified EVs (quantified by protein content) were combined with 1–2 nmol of synthetic microRNA inhibitor in 200 μL of electroporation buffer. The mixture was added into electroporation cuvette and pulsed once using a Gene Pulser Xcell™ system (Bio-Rad) under conditions ranging from 200 to 800 V and 50 to 150 μF. Following electroporation, samples were incubated at 37 °C for 30 min, and unincorporated anti-miRs were removed by ultracentrifugation.

2.7 Cell uptake experiments

To evaluate cellular uptake, primary neurons were seeded in 24-well plates and incubated with DiD-labeled SM-EVs for 4 h. After cells were fixed in 4% paraformaldehyde, permeabilized using phosphate buffered saline with Triton X-100 (PBST) for 1 h and stained with Phalloidin and DAPI, EV internalization was observed using confocal microscopy (Nikon AX, Japan).

2.8 Immunofluorescence staining

Primary neurons were fixed using 4% paraformaldehyde, permeabilized and blocked using PBST containing 5% bovine serum albumin (BSA) for 1 h. Samples were incubated at 4 °C for 12 h with anti-MAP2 and anti-Synapsin I. After PBS washes, samples were incubated at room temperature for 1 h with secondary antibodies. Images were acquired using a confocal microscope.

2.9 Western blot analysis

For western blot, BDNF, Synapsin I and postsynaptic density protein 95 (PSD95) antibodies were used at a dilution of 1:1000. Secondary antibodies were used for detection with ECL reagent, and band intensities were analyzed using ImageJ software. GAPDH served as the internal loading control.

2.10 *In vivo* distribution study

To assess biodistribution, S-EVs, M-EVs, SM-EVs and RVG-EVs were labeled with DiD or DiR (0.1 mg/mL). Mice were intravenously administered 50 μL of the labeled EVs and euthanized at 12, 24, 48, and 72 h. Brains were collected after PBS and 4% PFA perfusion, post-fixed in PFA for 12 h, cryoprotected in 30% sucrose and sectioned coronally at 25 μm.

Sections were permeabilized and blocked using PBST containing 5% BSA. Immunostaining was performed using anti-NeuN antibody followed by secondary antibody. Imaging was conducted on a Leica TCS SP8-MP confocal microscope.

2.11 Drug treatment

C57BL/6 mice were intravenously injected with anti-miRs, SM-EVs, or Anti-miRs@SM-EVs every two days for a total duration of one month.

2.12 Open field test (OFT)

To assess locomotion and anxiety-like behaviors, activities of mice were recorded for 10 min using a video camera linked to ANY-maze software. The arena was sanitized with 70% ethanol between tests.

2.13 Novel object recognition test (NORT)

To evaluate recognition memory, mice were acclimated to an empty arena (40 × 40 × 40 cm) under dim light for 5 min/day over 2 days. On training day, mice explored freely for 15 min with two objects placed in the arena. 1-h later, one of the objects was removed and a novel one was placed at the same position, then the mice exploration was recorded.

2.14 Y-maze test

The Y-maze, with three 30 cm arms set at 120°, was used to evaluate working memory. Mice were allowed to explore freely for 8 min. Arm entry sequences were recorded to determine spontaneous alternation behavior.

2.15 Morris water maze test

The entire experiment typically lasted six days. The mice were freed from a random area of the pool from days 1 to 5 and given 60 s to search and find the hidden platform. The experiment came to an end when the mice located the platform. The mice would be led to the platform and left there for 15 s if they couldn't locate it in 90 s. Mice were released into a new section after a one-hour break until all four sections had been completed. The delay between being released and discovering the platform was known as the escape latency, and it was noted. On day six, the mice were allowed to roam freely in the poor for ninety seconds after the hidden platform was removed from the water. The system examined the trajectory, escape latency, frequency of platform era crossings, and overall time spent in the targeted area.

2.16 Statistical analysis

Statistical data are presented as mean values with either standard deviation (SD) or standard error of the mean (SEM). All statistical assessments were carried out using GraphPad Prism software (version 8.0.2; GraphPad Software, San Diego, CA, USA). Differences between two independent groups were analyzed using a two-tailed, unpaired Student's t-test. For comparisons involving multiple groups, one-way analysis of variance (ANOVA) followed by appropriate post hoc testing was applied. A threshold of $P < 0.05$ was set to denote statistical significance. Significance levels were indicated as follows: $^{*}P < 0.05$, $^{**}P < 0.01$, $^{***}P < 0.001$, and $^{****}P < 0.0001$.

3 Results and discussion

3.1 Construction of Anti-miRs@SM-EVs

The construction of Anti-miRs@SM-EVs involved three sequential steps (Fig. 2(a)). First, 3T3-L1 cells were transfected with lentiviral vectors encoding SIRPα and MCAM to achieve co-overexpression of these brain-targeting proteins. We selected 3T3-L1 preadipocytes for two reasons. First, adipocyte-derived EVs have been previously shown to possess brain-entry capability and certain brain-targeting properties, which forms the basis of our study and does not require further validation. Second, using a cell line for targeted protein modification facilitates the production of engineered EVs with stable quality control. Then, stable celllines were selected using puromycin and blasticidin, with optimal antibiotic concentrations determined using CCK-8 assay (Fig. S1 in the Electronic Supplementary Material (ESM)). CLSM confirmed robust co-expression of SIRPα and MCAM with strong colocalization (Figs. 2(b) and 2(c)), Western blot analysis further validated increased expression levels of SIRPα and MCAM in transfected 3T3-L1 cells (Fig. 2(d) and Fig. S2 in the ESM), confirming the successful establishment of dually engineered stable cell lines.

Subsequently, the engineered 3T3-L1 cells were differentiated into mature adipocytes. Oil Red O staining confirmed that the transfection and antibiotic selection procedures did not impair their adipogenic differentiation capacity (Figs. 2(e) and 2(f), and Fig. S3 in the ESM). SM-EVs were then isolated from these cells via ultracentrifugation. EVs derived from non-engineered 3T3-L1 cells were used as control EVs (Ctrl-EVs). Nanoparticle tracking analysis (NTA) revealed that both Ctrl-EVs and SM-EVs had comparable hydrodynamic diameters (150 nm; Fig. 2(g)) and zeta potentials (−17 mV; Fig. 2(h)). Western blot confirmed the enrichment of SIRPα and MCAM on SM-EVs, along with the presence of classical EV markers (Figs. 2(i) and 2(j)). Subsequently, TEM confirmed that Anti-miRs@SM-EVs retained a typical spherical morphology with a double-membrane structure (Fig. 2(k)), with no significant changes in particle size or zeta potential (Fig. S4 in the ESM), indicating preserved structural integrity suitable for physiological applications. Finally, therapeutic anti-miRs were loaded into SM-EVs using electroporation. Fluorescence-based quantification showed a maximum encapsulation efficiency of 0.45 μg anti-miRs per mg EV protein under optimal electroporation parameters of 200 V and 50 μF (Fig. 2(l)).

3.2 The biocompatibility of Anti-miRs@SM-EVs

Prior to confirm the therapeutic efficacy of Anti-miRs@SM-EVs, we conducted a biocompatibility evaluation, including assessment of hemolysis and cytotoxicity. First, the hemolysis assay exhibited negligible hemolysis (< 5%) even at a 2 mg/mL concentration, indicating good blood compatibility of Anti-miRs@SM-EVs (Fig. 3(a)). Subsequently, we investigated the cytotoxicity by incubating HT22 cells with Anti-miRs@SM-EVs at various concentrations for 3 days. We found that cell viability remained above 90% across all concentrations, as determined by the CCK-8 test (Fig. 3(b)), confirming the non-toxic nature of the system within the tested range. We also demonstrated through CCK-8 assays that the cargo anti-miRs exhibited no significant cytotoxicity to the cells (Fig. S5 in the ESM). Meanwhile, living/dead staining by Calcein-AM/PI further supported the negligible cytotoxicity of Anti-miRs@SM-EVs (Fig. 3(c)). These results collectively suggest that Anti-miRs@SM-EVs exhibit favorable systemic biocompatibility.

Building on the biocompatibility of Anti-miRs@SM-EVs both *in vitro* and *in vivo*, we proceeded to assess their capability to alleviate synaptic loss and BNDF reduction at the cellular level. To assess the internalization efficiency of Anti-miRs@SM-EVs by primary neurons, DiD-labeled Anti-miRs@SM-EVs were co-cultured with primary neurons for 4 h. After removing unbound particles, CLSM revealed numerous DiD fluorescent signals localized predominantly in the perinuclear region (Figs. 3(d) and 3(e)), indicating successful internalization of Anti-miRs@SM-EVs by primary neurons.

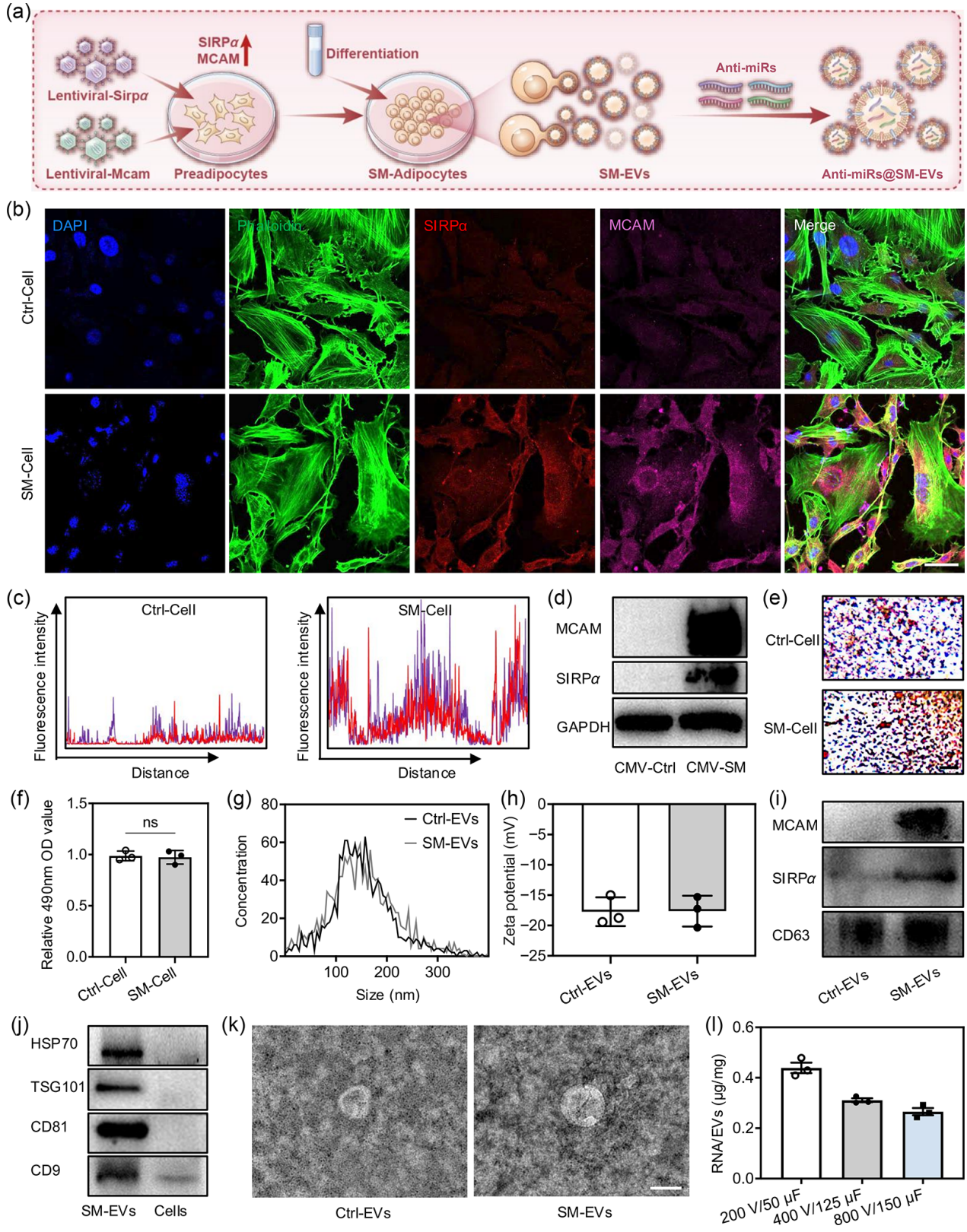

Figure 2 Preparation and characterization of SM-EVs. (a) Schematic illustrations of establishment of stable cell line and isolation of EVs. (b) Confocal microscopy images and (c) intensity analysis showing expression of SIRPα (red) and MCAM (magenta hot) in each cell lines. Scale bar = 50 μm. (d) Western blot analysis of SIRPα and MCAM expression. GAPDH serves as the loading control. Quantification of bands intensity was performed by densitometry. (e) Oil Red O staining of 3T3-L1 cell lines before and after adipogenic differentiation and (f) the relative quantitive analysis. Scale bar = 5 μm. (g) The size distribution of EVs measured by NTA. (h) Zeta potential of EVs measured by DLS. (i) Western blot analysis of SIRPα and MCAM expression on SM-EVs. (j) Western blot analysis of biomarkers of EVs expression. (k) Representative TEM images of EVs. (l) Loading efficiency of micoRNA inhibitor into SM-EVs via electroporation. Scale bar = 100 nm. All data are presented as mean ± SD, significance was determined using t tests (n = 3), ns: not significant.

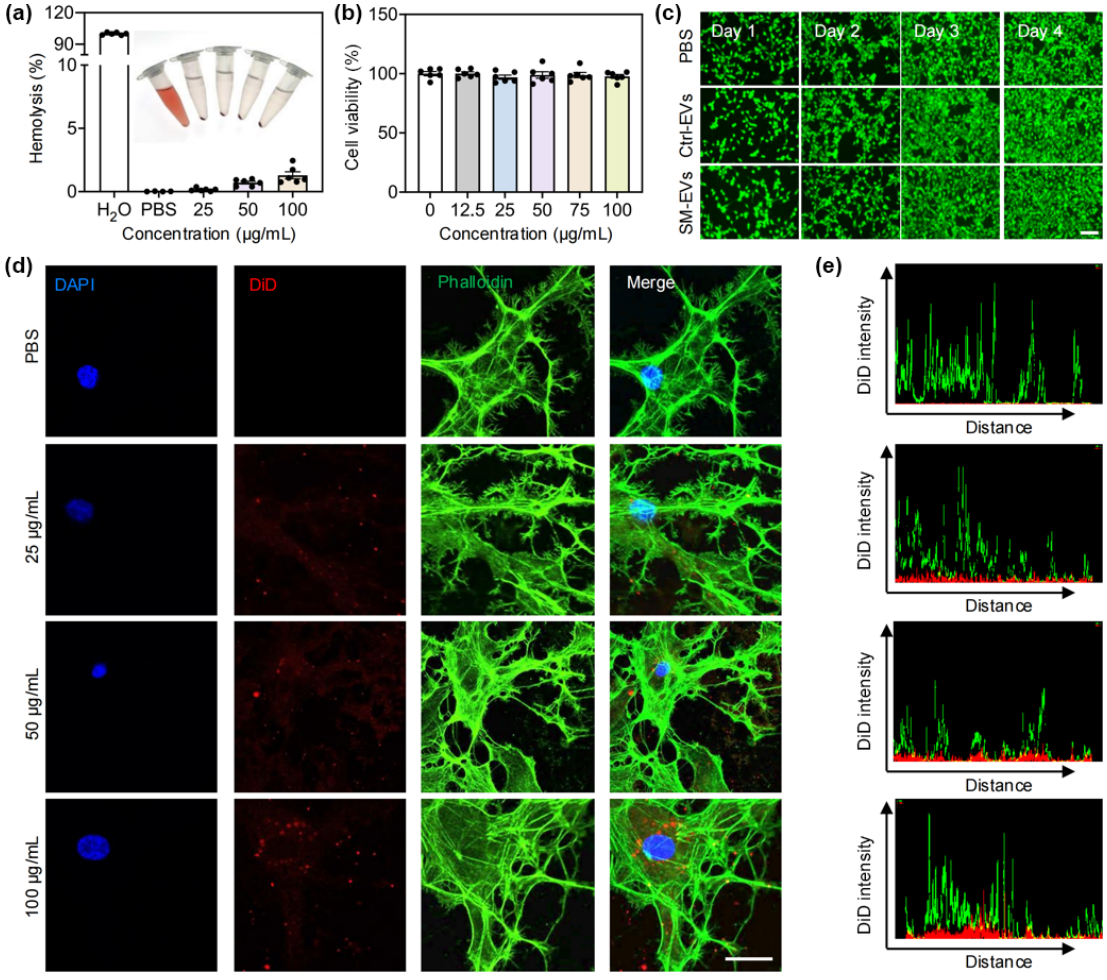

Figure 3 The biocompatibility of Anti-miRs@SM-EVs. (a) Hemolysis assay results of Anti-miRs@SM-EVs (n = 6). Inset: illustration of erythrocytes hemolysis. (b) Cell viability of HT22 cells co-cultured with Anti-miRs@SM-EVs, measured by CCK-8 (n = 6). (c) Living/dead fluorescence images of HT22 cells co-cultured with Anti-miRs@SM-EVs. Scale bar = 100 μm. (d) Confocal images showing the internalization of Anti-miRs@SM-EVs by primary neurons (blue: DAPI; red: DiD; green: phalloidin). Scale bar = 25 μm. (e) Fluorescence intensity indicates intracellular localization of EVs.

3.3 *In vitro* neuroprotective effects of Anti-miRs@SM-EVs

To evaluate the neuroprotective potential of Anti-miRs@SM-EVs, we used AT-EVs containing pathological microRNAs from diabetic mice to induce a synaptic loss and low BDNF model in primary neurons. Subsequently, PBS, Anti-miRs, SM-EVs and Anti-miRs@SM-EVs were applied to the damaged primary neurons to evaluate each of their capability to reverse synaptic deterioration. As shown in Figs. 4(a) and 4(b), treatment with Anti-miRs@SM-EVs exhibited the most pronounced restoration of BDNF levels compared to the SM-EVs and anti-miRs treatment groups. Figures 4(c) and 4(d) also indicated that treatment with Anti-miRs@SM-EVs significantly attenuated synaptic loss better than SM-EVs and anti-miRs treatment groups. These results collectively demonstrate that Anti-miRs@SM-EVs effectively internalize by primary neurons, exhibit potent neuroprotective effects against synaptic damage and promote the restoration of BDNF.

3.4 *In vivo* brain-targeting capability of Anti-miRs@SM-EVs

To evaluate the brain-targeting capability and biodistribution of Anti-miRs@SM-EVs across different brain regions, we also established the widely used RVG-modified EVs delivery system (RVG-EVs) as a control. As reported before, by fusing a part of peptide of rabies virus glycoprotein (RVG) to the exosomal membrane protein Lamp2b, RVG can enhance the brain targeting of EVs [42–45]. To construct this system, HEK-293t cells were transduced with a lentivirus vector encoding RVG-HA-EGFP. EGFP-positive HEK-293t cells were successfully identified by fluorescence microscope (Fig. S6 in the ESM). Western blot analysis confirmed high HA-tag expression in RVG-HEK-293t cells and their derived EVs (Figs. S7 and S8 in the ESM). The physical properties of RVG-EVs were characterized using DLS with a particle size of about 100 nm and a zeta potential of −20 mV (Fig. S9 in the ESM). Anti-miRs were then loaded into RVG-EVs via electroporation to construct Anti-miRs@RVG-EVs. To assess their biodistribution, DiR-labeled Anti-miRs@RVG-EVs were intravenously injected into C57BL/6 mice, and *in vivo* distribution was monitored using a fluorescence imaging system. As shown in Fig. S10 in the ESM, Anti-miRs@RVG-EVs exhibited significantly higher accumulation in the brain compared to Ctrl-EVs, confirming their enhanced brain-targeting capability.

After successfully generating Anti-miRs@RVG-EVs, we employed the same method to construct SIRPα-overexpressing EVs (SIRPα-EVs) and MCAM-overexpressing EVs (MCAM-EVs). C57BL/6 mice were intravenously administered DiR-labeled Anti-miRs@RVG-EVs, Anti-miRs@SIRPα-EVs, and Anti-

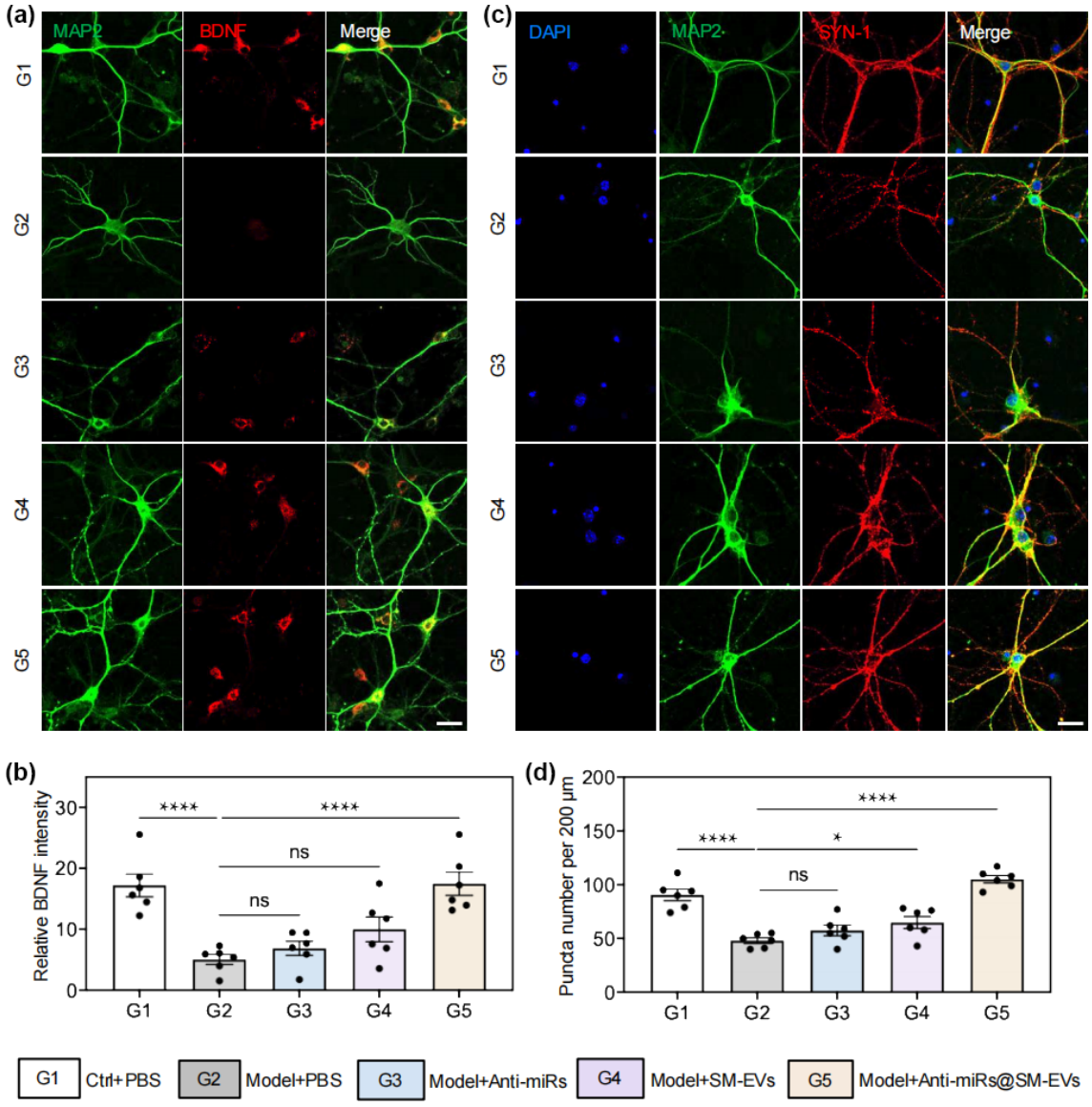

Figure 4 *In vitro* neuroprotective effects of Anti-miRs@SM-EVs. (a) Confocal images showing the expression of BDNF under different treatment conditions. (b) Quantification of BDNF intensity in MAP2-positive neurons. (c) Confocal images showing the expression of synaptic marker SYN-1 under different treatment conditions. (d) Quantification of SYN-1-positive puncta per 200 μm of MAP2-positive neurons. G1: PBS, G2: Model, G3: Anti-miRs, G4: SM-EVs, G5: Anti-miRs@SM-EVs. Scale bars = 20 μm. All data are presented as mean ± SD (n = 6).

miRs@MCAM-EVs respectively. The brain biodistribution of these vesicles was monitored using an *in vivo* fluorescence imaging system at predetermined time points. The results revealed that both SIRPα and MCAM facilitated independent brain-targeting capabilities. Specifically, Anti-miRs@SIRPα-EVs and Anti-miRs@MCAM-EVs showed approximately 2-fold and 3-fold increase in brain accumulation, respectively, compared to Anti-miRs@RVG-EVs (Figs. 5(a) and 5(c)). *Ex vivo* imaging was performed on excised brains, which confirmed the same trend (Fig. 5(d)). Subsequently, we evaluated the brain-targeting performance of Anti-miRs@SM-EVs. Notably, at all examined time points, Anti-miRs@SM-EVs exhibited higher fluorescence intensity than Anti-miRs@RVG-EVs, with a particularly pronounced enhancement up to 5-fold at 24- and 48-h post-injection (Figs. 5(b), 5(e) and 5(f)). These results suggest that Anti-miRs@SM-EVs possess superior BBB penetration compared to the widely used Anti-miRs@RVG-EVs system.

We further administered DiD-labeled Anti-miRs@SM-EVs and Anti-miRs@RVG-EVs intravenously into C57BL/6 mice and collected brain tissues for frozen sectioning to evaluate regional fluorescence intensity. Representative confocal microscopy images of major brain regions revealed a significantly higher uptake of Anti-miRs@SM-EVs compared to Anti-miRs@RVG-EVs at both 24- and 48-h post-injection, particularly in the hippocampus, hypothalamus, and cortex. Notably, the hippocampus exhibited an approximately 8-fold increase in Anti-miRs@SM-EVs uptake relative to Anti-miRs@RVG-EVs at 24 h (Figs. 6(a) and 6(c)), with a similar trend observed at 48 h (Figs. 6(b) and 6(d)). These findings confirm that SM-EVs possess enhanced CNS target efficiency and act as a more effective drug delivery vehicle than RVG-EVs.

3.5 *In vivo* therapeutic efficacy of Anti-miRs@SM-EVs

To evaluate the therapeutic efficacy of Anti-miRs@SM-EVs *in vivo*,

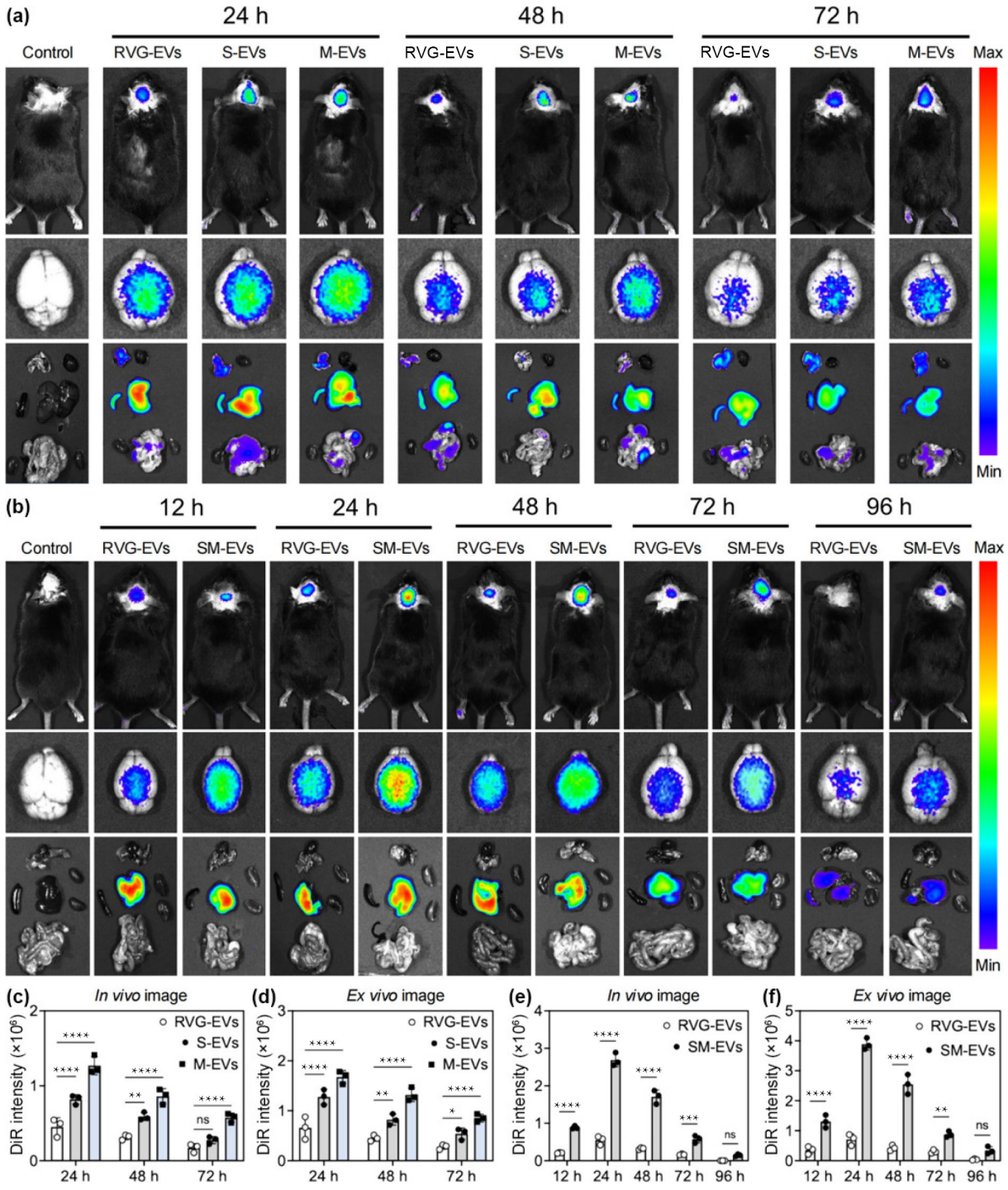

Figure 5 *In vivo* brain accumulation of Anti-miRs@SM-EVs after intravenous administration. (a) *In vivo* and *ex vivo* fluorescence images of mice brains after intravenous administration of Anti-miRs@RVG-EVs, Anti-miRs@SIRPα-EVs and Anti-miRs@MCAM-EVs. (b) *In vivo* and *ex vivo* fluorescence images of mice brains after intravenous administration of Anti-miRs@RVG-EVs and Anti-miRs@SM-EVs. Quantification of DiR intensity of RVG-EVs, SIRPα- EVs and MCAM-EVs at different timepoint (c) *in vivo* and (d) *ex vivo*. Quantification of DiR intensity of RVG-EVs and SM-EVs at different timepoint (e) *in vivo* and (f) *ex vivo*. All data are presented as mean ± SD, significance was determined using two-way ANOVA ($n = 3$), $^{*}P < 0.05$, $^{**}P < 0.01$, $^{***}P < 0.001$, $^{****}P < 0.0001$, ns: not significant.

we utilized both chow diet (CD) and high-fat diet (HFD) C57BL/6 mouse models. The experimental design, including model establishment, treatment regimen, and therapeutic assessment timeline, was illustrated in Fig. 7(a). Briefly, mice in CD group were fed with chow diet for 12 weeks, while mice in HFD, anti-miRs, SM-EVs, and Anti-miRs@SM-EVs groups received a high-fat diet for the same duration to induce diabetes and cognitive impairment. Following the dietary induction phase, mice in the HFD-related groups received intravenous injections of PBS, anti-miRs, SM-EVs, or Anti-miRs@SM-EVs every two days for a total of 4 weeks. Subsequently, behavioral tests were conducted to assess cognitive function, after that, all mice were sacrificed for further mechanistic studies.

As shown in Figs. 7(b) and 7(c), the OFT was first conducted to

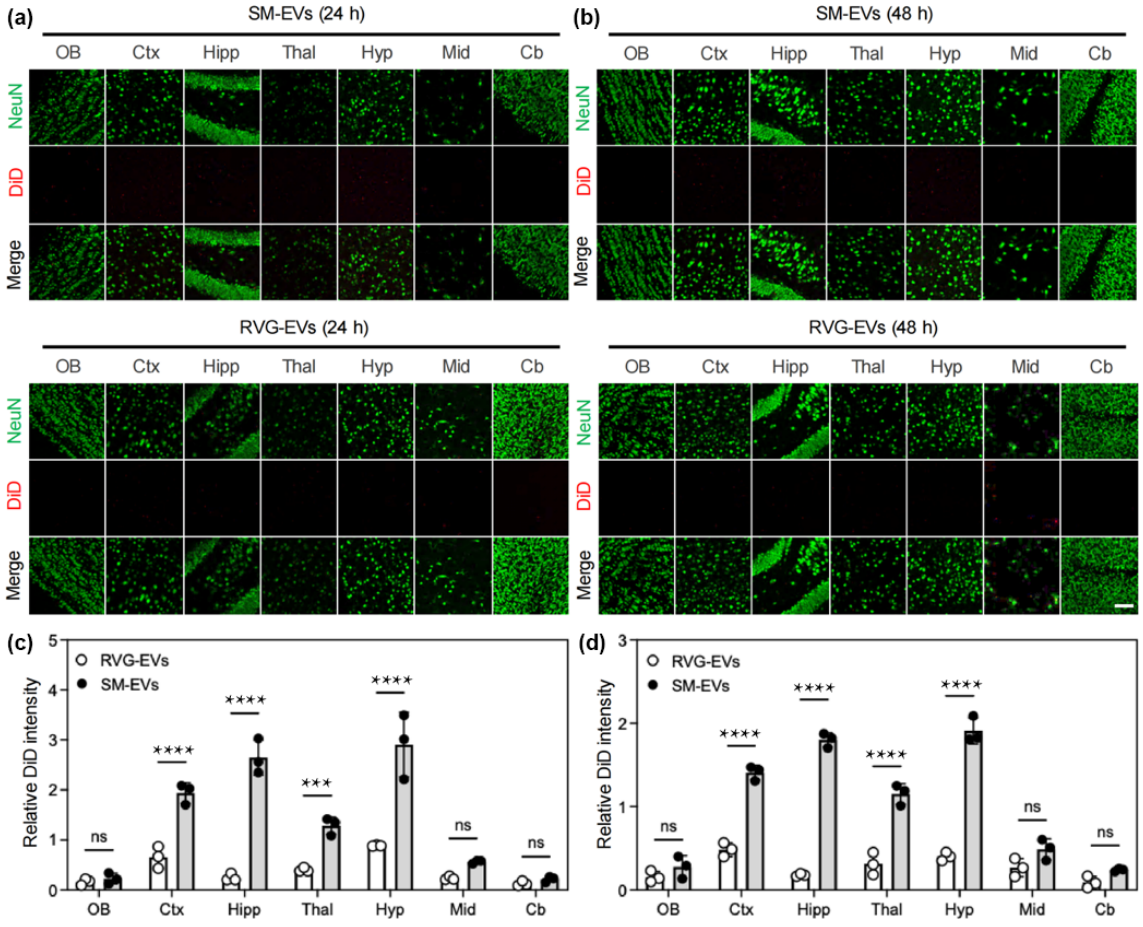

Figure 6 *In vivo* accumulation of Anti-miRs@SM-EVs in different brain regions after intravenous administration. Representative confocal images of DiD-labeled EVs and NeuN staining in different brain regions (a) 24 h or (b) 48 h after intravenous administration of Anti-miRs@RVG-EVs or Anti-miRs@SM-EVs (OB: olfactory bulb, Ctx: cortex, Hipp: hippocampus, Thal: thalamus, Hyp: hypothalamus, Mid: midbrain, Cb: cerebellum). Quantitative histograms showing the fluorescence intensity of DiD in different brain regions (c) 24 h or (d) 48 h after injection. Scale bar = 75 μm. All data are presented as mean ± SD, significance was determined using two-way ANOVA ($n = 3$), ***$P < 0.001$, ****$P < 0.0001$, ns: not significant.

ensure that none of the mice exhibited anxiety-like behavior. The total distance traveled, and time spent in the central area indicated that HFD, anti-miRs, or SM-EVs did not negatively affect the anxiety levels or motor abilities of the mice.

For evaluation of memory and spatial learning, Morris water maze (MWM) testing was performed. We analyzed trajectory maps, escape latency, total time mice spent in target quadrant, and platform crossing frequency post-treatment. Representative motion trajectories are shown in Fig. 7(d). Mice treated with Anti-miRs@SM-EVs exhibited the shortest escape latencies (Figs. 7(e) and 7(f)), spent the most time in target quadrant (Fig. 7(g)), and had the highest frequency of platform crossings (Fig. 7(h)), outperforming both the anti-miRs and SM-EVs groups. Then the Y-maze and NORT were performed. The Y-maze results revealed that the Anti-miRs@SM-EVs group demonstrated significantly improved short-term memory compared to the SM-EVs and anti-miRs groups (Fig. 7(i)). Similarly, NORT results showed enhanced novel object preference in the Anti-miRs@SM-EVs group (Fig. 7(j)). These improvements are likely attributed to the synergistic effects of SM-EVs and its anti-miRs cargos.

Although RNA typically could not cross the BBB, when encapsulated in EVs, anti-miR-9-3p, anti-miR-9b-5p, anti-miR-140-5p, and anti-miR-7b-5p significantly reduced pathogenic microRNA levels in the hippocampus, thereby alleviating spatial learning and memory impairments. Interestingly, HFD mice treated with control adipose tissue-derived EVs (AT-EVs) also showed reduced escape latencies and increased time in the target quadrant, suggesting that EVs and their cargos from normal adipocytes may exert beneficial effects on neuronal function. Although the specific identities of these active cargos remain unknown, ongoing efforts are being made to identify the microRNAs or proteins responsible for these neuroprotective effects.

In summary, the data collectively demonstrate that intravenous administration of Anti-miRs@SM-EVs effectively improves cognitive impairment in diabetic mice.

3.6 Illustration of the therapeutic mechanism of anti-miRs@SM-EVs

Finally, to further explore the underlying therapeutic mechanisms, we detected microRNAs level and markers associated with synaptic integrity. The pathogenic microRNAs — miR-9-3p, miR-9b-5p, miR-140-5p, and miR-7b-5p, were quantified. These microRNAs in hippocampus contribute to cognitive impairment by negatively regulate expression of genes associated with synapse formation and plasticity, such as *BDNF*, *Prox1*, *ADAM10*, *Wnt1*, *SORBS2* and

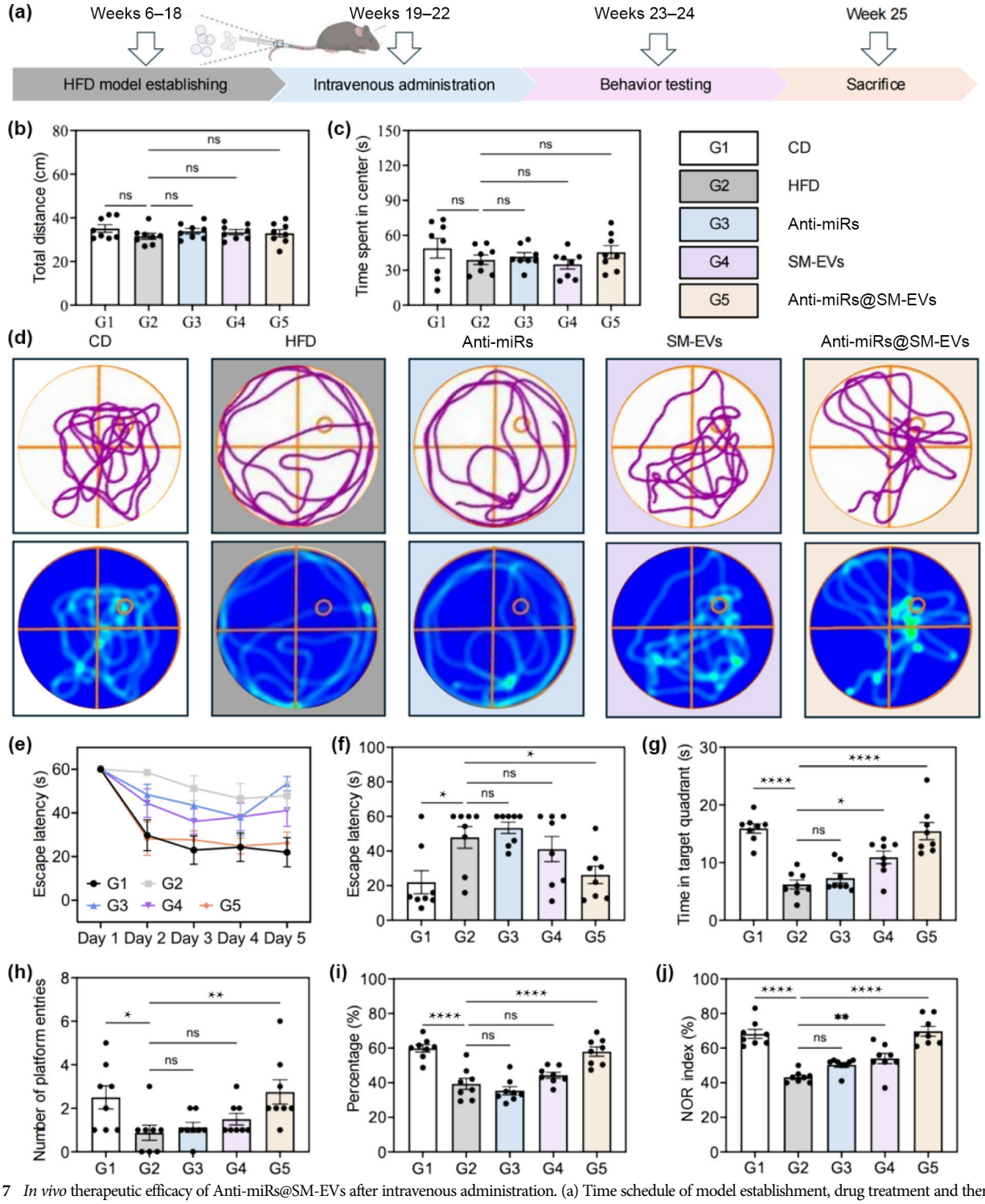

Figure 7 *In vivo* therapeutic efficacy of Anti-miRs@SM-EVs after intravenous administration. (a) Time schedule of model establishment, drug treatment and therapeutic assessment. (b) Total distance travelled in OFT. (c) Time spent in center in OFT. (d) Representative swimming trajectories and heatmaps of mice in MWM. (e) and (f) Escape latency to the platform in MWM. (g) Time spent in target quadrant in MWM. (h) Number of platform entries in MWM. (i) Percentage of spontaneous alternation in Y-maze test. (j) Novel object recognition index in NORT. All data are presented as mean ± SEM, significance was determined using two-way ANOVA (n = 8), *P < 0.05, **P < 0.01, ****P < 0.0001, ns: not significant.

TCF12 [8, 46–48]. As shown in Figs. 8(a)–8(d), treatment with Anti-miRs@SM-EVs significantly reduced the expression of all four microRNAs in the hippocampus.

In addition, we evaluated the expression of BDNF and key synaptic integrity markers, Synapsin-1 (SYN-1) and PSD95. Western blotting showed that the levels of BDNF, SYN-1, and PSD95 were markedly elevated compared with those in the HFD group (Fig. 8(e)). Immunofluorescence staining confirmed these findings (Fig. 8(f)), collectively indicating a substantial attenuation of synaptic loss and neuronal damage. Among all treatment groups, Anti-miRs@SM-EVs exhibited the strongest therapeutic effect,

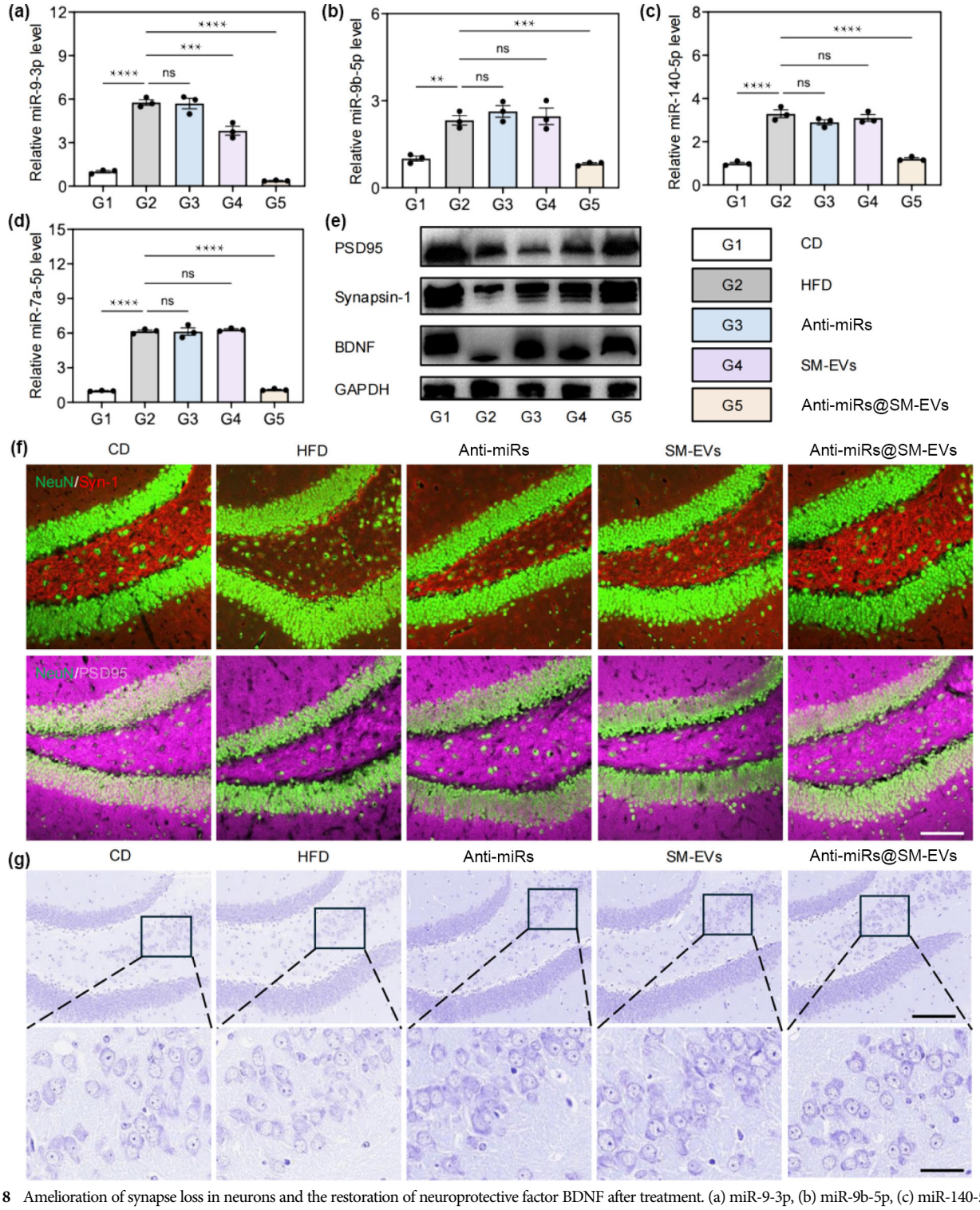

Figure 8 Amelioration of synapse loss in neurons and the restoration of neuroprotective factor BDNF after treatment. (a) miR-9-3p, (b) miR-9b-5p, (c) miR-140-5p, and (d) miR-7a-5p concentrations in hippocampus using qPCR, U6 served as the loading control. (e) Western blot analysis of PSD95, Synapsin-1 and BDNF expression in hippocampus. GAPDH served as the loading control. (f) Immunofluorescence intensity of SYN-1 and PSD95 in hippocampus. Scale bar: 100 μm. (g) Nissl staining of the hippocampus. Scale bars: 100 μm (upper) and 25 μm (down). All data are presented as mean ± SD, significance was determined using two-way ANOVA ($n = 3$), $^{**}P < 0.01$, $^{****}P < 0.0001$, ns: not significant.

highlighting the benefit of a synergistic therapeutic strategy.

To evaluate biocompatibility, Nissl staining was performed (Fig. 8(g)). Furthermore, systemic toxicity was assessed by monitoring blood biochemical parameters, body weight, and conducting histopathological analysis. Importantly, four weeks of continuous treatment did not result in negative changes in blood biochemical indices or body weight (Figs. S11 and S12 in the ESM), nor did it cause noticeable pathological alterations in major organs, as shown by H&E staining (Fig. S13 in the ESM).

Collectively, these results demonstrate that intravenous

administration of Anti-miRs@SM-EVs achieves excellent therapeutic efficacy in neuroprotection, with minimal systemic toxicity and high biocompatibility.

4 Conclusions

In this study, we developed a brain-targeted RNA delivery platform using dual-engineered adipocyte-derived EVs loaded with a combination of four anti-miRs targeting pathogenic microRNAs implicated in diabetes-induced cognitive impairment. Our results demonstrated that Anti-miRs@SM-EVs effectively protected primary neurons from synaptic damage induced by these pathogenic microRNAs. *In vivo*, SM-EVs exhibited markedly superior brain accumulation compared to the widely used RVG-EVs delivery system. Notably, owing to their adipose-derived origin, SM-EVs preferentially accumulated in metabolism-related brain regions, including the hippocampus, hypothalamus, and cortex, suggesting additional potential for metabolic regulation.

In a diabetic mouse model, four weeks of intravenous administration of Anti-miRs@SM-EVs significantly reduced levels of the four pathogenic microRNAs [8], thereby reversing synaptic loss and restoring BDNF expression, ultimately leading to improved cognitive performance [46–48]. These findings support the therapeutic potential of this brain-targeted RNA delivery system as a combinatorial treatment strategy for diabetes-induced cognitive impairment.

Given that approximately 98% of small-molecule drugs are impeded by the BBB and no effective targeted therapy currently exists for diabetes-induced cognitive impairment, the novelty of our work lies in the construction of a dual-targeted EV delivery platform. This platform not only achieves nearly 5-fold higher brain-targeting efficiency compared to RVG-EVs, but also enables the co-delivery of four anti-miRs for multifactorial synergistic intervention. By leveraging advances in EV engineering, our approach addresses current limitations in brain drug delivery, including low targetability, poor biocompatibility, and limited cargo stability.

This study specifically aimed to determine whether SM-EVs could surpass existing brain delivery systems in BBB penetration and whether the co-delivery of multiple anti-miRs could result in effective accumulation and therapeutic outcomes in the brain. Our results clearly demonstrated that diabetic mice treated with Anti-miRs@SM-EVs exhibited reduced synaptic injury, restoration of BDNF levels, and significantly improved cognitive function relative to other treatment groups. These outcomes underscore the efficacy and advantages of our synergistic therapeutic strategy.

Electronic Supplementary Material: Supplementary material (dose–response killing curves in 3T3-L1 cells; quantification of expression of SIRPα and MCAM between control and stable cell lines; morphological changes of 3T3-L1 cells during adipogenic differentiation observed under a light microscope; characterization of SM-EVs before and after electroporation; cell viability of HT22 cells co-cultured with cargo Anti-miRs; fluorescence microscopy image of EGFP expression in HEK293T cells; Western blot analysis of HA-Flag expression on RVG-EVs; quantification of expression of HA-tag on RVG-EVs; characterization of RVG-EVs; *in vivo* accumulation of Anti-miRs@RVG-EVs in brain after intravenous administration; blood biochemical indices of each group, with reference ranges indicated in parentheses; body weight of experimental groups; H&E staining of the major organs) is available in the online version of this article at https://doi.org/10.26599/NR.2026.94908479.

Data availability

The original contributions presented in the study are included in the article and the Electronic Supplementary Material, further inquiries can be directed to the corresponding author.

Acknowledgements

This work was supported by Noncommunicable Chronic Diseases-National Science and Technology Major Project (Nos. 2024ZD0523200 and 2023ZD0507903), the National Natural Science Foundation of China Grant Awards (Nos. 82450002, 82030026, 82270883, 82470865, and 32201088), the National Chinese-Western Medicine Clinical Collaboration Project for Major Difficult Diseases, the Key Research and Development Program of Jiangsu Province of China (Nos. BE2023774 and BE2022853), the Fundamental Research Funds for the Central Universities (No. 14380546), and the Multidisciplinary Joint Innovation and Tackling New Technology Project from the Affiliated Drum Tower Hospital, Medical School of Nanjing University.

Declaration of competing interest

The authors declare no conflicts of interest.

Author contribution statement

J. W., Y. J. Z, and Y. B. designed the study. X. T. C., H. X. S., and Z. C. Z. performed the study. X. T. C. wrote the draft of the paper. J. Y. C. and J. W. contributed to reviewing and revising the paper. J. Y. C., Y. J. Z., Y. B. and J. W. are the corresponding authors. All authors read and approved the final version of the manuscript. All authors confirm that they had full access to all the data in the study and accept responsibility to submit the paper for publication.

Informed consent

Not applicable.

Ethics statement

The animal experiments were carried out following the guidelines of Nanjing Drum Tower Hospital for the Care and Use of Laboratory Animals and were approved by the Committee on Ethical Use of Animals of Nanjing Drum Tower Hospital (No. 20240614).

Use of AI statement

None.

References

[1] Gustafson, D. Adiposity indices and dementia. *Lancet Neurol.* **2006**, *5*, 713–720.

[2] Cukierman-Yaffe, T.; Gerstein, H. C.; Colhoun, H. M.; Diaz, R.; García-Pérez, L. E.; Lakshmanan, M.; Bethel, A.; Xavier, D.; Probstfield, J.; Riddle, M. C. et al. Effect of dulaglutide on cognitive impairment in type 2 diabetes: An exploratory analysis of the REWIND trial. *Lancet Neurol.* **2020**, *19*, 582–590.

[3] Biessels, G. J.; Nobili, F.; Teunissen, C. E.; Simó, R.; Scheltens, P. Understanding multifactorial brain changes in type 2 diabetes: A biomarker perspective. *Lancet Neurol.* **2020**, *19*, 699–710.

[4] O'Brien, P. D.; Hinder, L. M.; Callaghan, B. C.; Feldman, E. L. Neurological consequences of obesity. *Lancet Neurol.* **2017**, *16*, 465–477.
[5] McCrimmon, R. J.; Ryan, C. M.; Frier, B. M. Diabetes and cognitive dysfunction. *Lancet* **2012**, *379*, 2291–2299.
[6] Srikanth, V.; Sinclair, A. J.; Hill-Briggs, F.; Moran, C.; Biessels, G. J. Type 2 diabetes and cognitive dysfunction-towards effective management of both comorbidities. *Lancet Diabetes Endocrinol.* **2020**, *8*, 535–545.
[7] Lin, X.; Cai, L. J.; Cao, X. Y.; Zhao, Y. J. Stimuli-responsive silk fibroin for on-demand drug delivery. *Smart Med.* **2023**, *2*, e20220019.
[8] Wang, J.; Li, L.; Zhang, Z.; Zhang, X. H.; Zhu, Y.; Zhang, C. Y.; Bi, Y. Extracellular vesicles mediate the communication of adipose tissue with brain and promote cognitive impairment associated with insulin resistance. *Cell Metab.* **2022**, *34*, 1264–1279.e8.
[9] Hu, X. J.; Liu, R.; Zhang, C.; Wang, Y. Z.; Wei, R. Y.; Kong, B.; Zhou, X. T.; Li, M. Y. Human corneal lenticules decorated with mesenchymal-stem-cells-encapsulated microneedles for cornea stroma regeneration. *ACS Nano* **2025**, *19*, 26500–26513.
[10] Wang, J.; Cai, L. J.; Li, N.; Luo, Z. Q.; Ren, H. Z.; Zhang, B.; Zhao, Y. J. Developing mRNA nanomedicines with advanced targeting functions. *Nano-Micro Lett.* **2025**, *17*, 155.
[11] Wang, J.; Zhu, H. F.; Gan, J. J.; Liang, G. F.; Li, L.; Zhao, Y. J. Engineered mRNA delivery systems for biomedical applications. *Adv. Mater.* **2024**, *36*, 2308029.
[12] Wang, Y. W.; Cai, L. J.; Zhang, Y. Y.; Cong, Y.; Zhao, Y. J. Natural matrine-integrated pollen delivery systems for allergic contact dermatitis treatment. *Smart Med.* **2025**, *4*, e136.
[13] Kim, H.; Lee, Y. Y.; Kim, V. N. The biogenesis and regulation of animal microRNAs. *Nat. Rev. Mol. Cell Biol.* **2025**, *26*, 276–296.
[14] Rupaimoole, R.; Slack, F. J. MicroRNA therapeutics: Towards a new era for the management of cancer and other diseases. *Nat. Rev. Drug Discov.* **2017**, *16*, 203–222.
[15] Kim, K. Y. RNA therapy: Rich history, various applications and unlimited future prospects. *Exp. Mol. Med.* **2022**, *54*, 455–465.
[16] Huang, X. G.; Kong, N.; Zhang, X. C.; Cao, Y. H.; Langer, R.; Tao, W. The landscape of mRNA nanomedicine. *Nat. Med.* **2022**, *28*, 2273–2287.
[17] Huang, D. Q.; Cai, L. J.; Li, N.; Zhao, Y. J. Ultrasound-trigged micro/nanorobots for biomedical applications. *Smart Med.* **2023**, *2*, e20230003.
[18] Luo, W.; Chen, C.; Guo, X. H.; Guo, X.; Zheng, J.; Liu, J.J.; Fan, X. D.; Luo, M.; Yu, Z.; Li, H. G. et al. Critical challenges of intravenous nanomaterials crossing the blood-brain barrier: from blood to brain. *Adv. Funct. Mater.* **2025**, *35*, 2409522.
[19] Wu, D.; Chen, Q.; Chen, X. J.; Han, F.; Chen, Z.; Wang, Y. The blood-brain barrier: Structure, regulation and drug delivery. *Sig. Transduct. Target. Ther.* **2023**, *8*, 217.
[20] Cai, R. W.; Miao, S. S.; Cao, X. Y.; Nie, M.; Zhao, Y. J. Freeze-derived anisotropic porous microparticles for engineered mesenchymal stem cell loading and wound healing. *Research* **2025**, *8*, 0668.
[21] Zhang, W. Y.; Cai, L. J.; Gan, J. J.; Zhao, Y. J. Photothermal responsive porous hollow microneedles as Chinese medicine versatile delivery system for wound healing. *Smart Med.* **2024**, *3*, e20240007.
[22] Gao, J. J.; Xia, Z. T.; Gunasekar, S.; Jiang, C.; Karp, J. M.; Joshi, N. Precision drug delivery to the central nervous system using engineered nanoparticles. *Nat. Rev. Mater.* **2024**, *9*, 567–588.
[23] Masserini, M. Nanoparticles for brain drug delivery. *ISRN Biochem.* **2013**, *2013*, 238428.
[24] Hu, X. J.; Kong, B.; Wang, Y. Z.; Zhao, Y. J.; Li, M. Y.; Zhou, X. T. Responsive porous microneedles with riboflavin ocular microinjection capability for facilitating corneal crosslinking. *J. Nanobiotechnol.* **2024**, *22*, 588.
[25] Zhang, Y. S.; Khademhosseini, A. Advances in engineering hydrogels. *Science* **2017**, *356*, eaaf3627.
[26] Hassan, S.; Prakash, G.; Bal Ozturk, A.; Saghazadeh, S.; Sohail, M. F.; Seo, J.; Dokmeci, M. R.; Zhang, Y. S.; Khademhosseini, A. Evolution and clinical translation of drug delivery nanomaterials. *Nano Today* **2017**, *15*, 91–106.
[27] Lv, H. L.; Yao, Y. X.; Yuan, M. Y.; Chen, G. Y.; Wang, Y. C.; Rao, L. J.; Li, S. C.; Kara, U. I.; Dupont, R. L.; Zhang, C. et al. Functional nanoporous graphene superlattice. *Nat. Commun.* **2024**, *15*, 1295.
[28] Zhang, J. H.; Ji, C.; Zhang, H. B.; Shi, H.; Mao, F.; Qian, H.; Xu, W. R.; Wang, D. Q.; Pan, J. M.; Fang, X. J. et al. Engineered neutrophil-derived exosome-like vesicles for targeted cancer therapy. *Sci. Adv.* **2022**, *8*, eabj8207.
[29] Zhao, Z. Y.; Wang, Z.; Li, G.; Cai, Z. W.; Wu, J. Z.; Wang, L.; Deng, L. F.; Cai, M.; Cui, W. G. Injectable microfluidic hydrogel microspheres for cell and drug delivery. *Adv. Funct. Mater.* **2021**, *31*, 2103339.
[30] Greening, D. W.; Xu, R.; Rai, A.; Suwakulsiri, W.; Chen, M. S.; Simpson, R. J. Clinical relevance of extracellular vesicles in cancer-therapeutic and diagnostic potential. *Nat. Rev. Clin. Oncol.* **2025**, *22*, 924–952.
[31] Hu, Z. Y.; Qian, S. T.; Zhao, Q. Y.; Lu, B. L.; Lu, Q.; Wang, Y. H.; Zhang, L. C.; Mao, X. Y.; Wang, D. R.; Cui, W. G. et al. Engineering strategies for apoptotic bodies. *Smart Med.* **2024**, *3*, e20240005.
[32] Wei, X. W.; Zhang, D. G.; Zhu, Y. F. Exosomes: Toward a potential application in bladder cancer diagnosis and treatment. *Smart Med.* **2024**, *3*, e20230027.
[33] Wang, J.; Zhang, X. H.; Zhu, Y.; Sun, H. X.; Chen, X. T.; Zhao, Z. C.; Zhang, N. N.; Zhang, C. Y.; Li, L.; Bi, Y. Adipocyte-derived extracellular vesicles are key regulators of central leptin sensitivity and energy homeostasis. *Cell Metab.* **2026**, *38*, 82–99.e8.
[34] Qi, C.; Ma, X. D.; Zeng, Q.; Huang, Z. W.; Zhang, S. S.; Deng, X. K.; Kong, T. T.; Liu, Z. Multicompartmental coacervate-based protocell by spontaneous droplet evaporation. *Nat. Commun.* **2024**, *15*, 1107.
[35] Luo, G. Y.; Yu, Y. F.; Yuan, Y. X.; Chen, X.; Liu, Z.; Kong, T. T. Freeform, reconfigurable embedded printing of all-aqueous 3D architectures. *Adv. Mater.* **2019**, *31*, 1904631.
[36] Zhang, X. X.; Chen, G. P.; Zhang, H.; Shang, L. R.; Zhao, Y. J. Bioinspired oral delivery devices. *Nat. Rev. Bioeng.* **2023**, *1*, 208–225.
[37] Ge, K. Z.; Bai, Z. T.; Wang, J. W.; Li, Z.; Gao, F. F.; Liu, S. N.; Zhang, L.; Gao, F. L.; Xie, C. M. Engineering EVs-mediated mRNA delivery regulates microglia function and alleviates depressive-like behaviors. *Adv. Mater.* **2025**, *37*, 2418872.
[38] Yang, C. H.; Xue, Y. X.; Duan, Y.; Mao, C.; Wan, M. M. Extracellular vesicles and their engineering strategies, delivery systems, and biomedical applications. *J. Control. Release* **2024**, *365*, 1089–1123.
[39] Rehman, F. U.; Liu, Y.; Zheng, M.; Shi, B. Y. Exosomes based strategies for brain drug delivery. *Biomaterials* **2023**, *293*, 121949.
[40] Zhang, Z. H.; Yang, X. Y.; Zhao, Y. J.; Ye, F. F.; Shang, L. R. Liquid crystal materials for biomedical applications. *Adv. Mater.* **2023**, *35*, 2300220.
[41] Zhang, X.; Zhang, H. B.; Gu, J. M.; Zhang, J. Y.; Shi, H.; Qian, H.; Wang, D. Q.; Xu, W. R.; Pan, J. M.; Santos, H. A. Engineered extracellular vesicles for cancer therapy. *Adv. Mater.* **2021**, *33*, e2005709.
[42] Alvarez-Erviti, L.; Seow, Y.; Yin, H. F.; Betts, C.; Lakhal, S.; Wood, M. J. A. Delivery of siRNA to the mouse brain by systemic injection of targeted exosomes. *Nat. Biotechnol.* **2011**, *29*, 341–345.
[43] Kim, J. Y.; Choi, W. I.; Kim, Y. H.; Tae, G. Brain-targeted delivery of protein using chitosan- and RVG peptide-conjugated, pluronic-based nano-carrier. *Biomaterials* **2013**, *34*, 1170–1178.
[44] Han, Y.; Gao, C. H.; Wang, H.; Sun, J. J.; Liang, M.; Feng, Y.; Liu, Q. Q.; Fu, S. Y.; Cui, L.; Gao, C. S. et al. Macrophage membrane-coated nanocarriers Co-Modified by RVG29 and TPP improve brain neuronal mitochondria-targeting and therapeutic efficacy in Alzheimer's disease mice. *Bioact. Mater.* **2021**, *6*, 529–542.
[45] Cui, G. H.; Guo, H. D.; Li, H.; Zhai, Y.; Gong, Z. B.; Wu, J.; Liu, J.

S.; Dong, Y. R.; Hou, S. X.; Liu, J. R. RVG-modified exosomes derived from mesenchymal stem cells rescue memory deficits by regulating inflammatory responses in a mouse model of Alzheimer's disease. *Immun. Ageing* **2019**, *16*, 10.

[46] Wang, H.; Zhang, L.; Yang, W. Y.; Ji, X. Y.; Gao, A. Q.; Wei, Y. H.; Ding, X.; Kang, Y.; Ding, J. H.; Fan, Y. et al. Visceral adipose tissue-derived extracellular vesicles promote stress susceptibility in obese mice via miR-140-5p. *Acta Pharmacol. Sin.* **2025**, *46*, 1221–1235.

[47] Sun, X. J.; Chen, Y. X.; Zhang, Y.; Cheng, T. T.; Peng, H. S.; Sun, Y. T.; Liu, J. G.; Xu, C. Exosomes released from immature neurons regulate adult neural stem cell differentiation through microRNA-7a-5p. *Stem Cells* **2025**, *43*, sxae082.

[48] Ma, N. N.; Pan, J.; Ye, X. Y.; Yu, B.; Zhang, W.; Wan, J. Whole-transcriptome analysis of APP/PS1 mouse brain and identification of circRNA-miRNA-mRNA networks to investigate AD pathogenesis. *Mol. Ther. Nucleic Acids* **2019**, *18*, 1049–1062.